



Research Article

Characterization of Controlled Release Microspheres Using FIB-SEM and Image-Based Release Prediction

Shawn Zhang,^{1,3} Dan Wu,² and Liping Zhou¹

Received 11 April 2020; accepted 22 June 2020; published online 14 July 2020

Abstract. For polymer-based controlled release drug products (e.g. microspheres and implants), active pharmaceutical ingredient distribution and microporosity inside the polymer matrix are critical for product performance, particularly drug release kinetics. Due to the decreasing domain size and increasing complexity of such products, conventional characterization and release test techniques are limited by their resolution and speed. In this study, samples of controlled release poly(lactic-co-glycolic acid) microspheres in the diameter range of 30–80 μm are investigated with focused ion beam scanning electron microscope imaging at 20 nm or higher resolution. Image data is quantified with artificial intelligence-based image analytics to provide size distributions of drug particles and pores within the microsphere sample. With an innovative image-based numerical simulation method, release profiles are predicted in a matter of days regardless of the designed release time. A mechanistic understanding on the impact of porosity to the interplays of drug, formulation, process, and dissolution was gained.

KEY WORDS: Focused ion beam scanning electron microscopy; Image-based release simulation; Drug particle inside microsphere; Microporosity; Quantitative characterization.

INTRODUCTION

Controlled release (CR) drug products have been developed to meet specific therapeutic targets, control toxicology effects, and improve patient compliance. They are typically formulated using carrier(s) of specific physical and chemical properties, such as biodegradable poly(lactic-co-glycolic acid) (PLGA) (1,2). The active pharmaceutical ingredient (API) is dispersed into the PLGA matrix to achieve a desirable release profile. *In vitro* release testing methods, necessary for product development, batch release of product, and *in vitro-in vivo* correlations, typically require significant effort for the development of appropriate assays and analytical methods (3). Additionally, if accelerated *in vitro* testing methods are not available, the time required for batch release of long-acting drug products, sometimes up to several months or years, can be problematic for the development and commercialization. Furthermore, due to their microscale domain size and increasing complexity, polymeric controlled release formulations are challenging to characterize by conventional analytical methods. For exam-

ple, microspheres used in a controlled release (CR) formulation are often 30–80 μm in diameter. To ensure sustained release over a period of weeks or months, API domains or the microporous network in a microsphere are often as small as a few tens of nanometers (4,5). Bulk measurements often fail to reveal the mechanisms of drug-formulation-process-dissolution interplay complicated by small domain size. Conventional particle imaging techniques such as confocal microscopy, Raman imaging (6), and X-Ray micro-computed tomography (7–9) lack the required resolution to resolve small API and porosity domains inside a microsphere. Consequently, the development of alternative approaches to understand the essential quality microstructure attributes that affect drug release and performance are of critical importance. Electron microscopy (EM) stands out as an indispensable tool in CR drug characterization to reveal the properties of the internal microstructures of microsphere samples, such as API domain size distribution and microporosity, and correlate them with the bulk behavior. The most commonly used microscopy techniques for examining the shape and the morphology of the matrix include transmission electron microscopy (TEM) (10) and scanning electron microscopy (SEM) (11,12). Although sufficiently high resolution is achievable by these EM platforms, their investigations are limited to either the particle surface or a very thin slice of the sample. While cryo-cleaved cross-sectioning (10) makes it possible to image the inside of a particle, mechanical damage is typically produced during the

¹ DigiM Solution LLC, 67 South Bedford Street, Suite 400 West, Burlington, Massachusetts 01803, USA.

² Bausch Health Companies, 400 Somerset corporate Blvd, Bridgewater, New Jersey 08807, USA.

³ To whom correspondence should be addressed. (e-mail: shawn.zhang@digiminsolution.com)

process, preventing accurate and quantitative investigation of the internal microstructures.

Focused Ion Beam (FIB) SEM is a new-generation electron microscopy imaging platform that supports 3D nano-tomography imaging. Gallium ion FIB can remove material from the sample at a precision as high as a few nanometers without disrupting microstructures in the next layer (13). A clean, artifact-free cross-section can thus be prepared for high-resolution field emission SEM imaging. Iterative FIB milling and SEM imaging at 3–50 nm resolution produces a stack of SEM images that can be reconstructed into a 3D volume. Chemical composition can be confirmed using energy dispersion X-ray spectroscopy (EDS) (14).

Image-based analytics have been demonstrated as a valuable technique for the characterization of complex pharmaceutical systems (4,6,7). Due to the limited image data of microsphere formulations, quantitative analysis and modeling, essential to understand the role of the microstructures in the drug-formulation-process-dissolution interplay, is sparse at best. Further, investigations of the relationship between microstructures and API release are limited.

In this paper, we describe an innovative image-based characterization method for PLGA microsphere characterization. FIB-SEM provided the necessary high resolution to visualize the API and microporosity morphology inside microsphere samples. API particle distribution uniformity and pore morphology were qualitatively assessed. An artificial intelligence (AI)-based algorithm further segmented the images into different material phase domains. Quantitative information was computed including volume fractions, spatial distribution homogeneity, and particle/pore size distributions (15). An image-based release simulation algorithm predicted monolithic release profiles using the drug distribution extracted from microsphere FIB-SEM images. The impact of microporosity was investigated to demonstrate this approach as a powerful and time-efficient alternative for CR microsphere performance characterization.

METHODS

Materials

Microsphere drug samples were formulated using PLGA polymer and compound A, the API. Poly(D, L-lactide-co-glycolide) (50:50 lactic acid: glycolic acid; inherent viscosity: 0.44 dL/g) was obtained from Evonik Industries (Darmstadt, Germany). Compound A was purchased from Cipan (Castanheira do Ribatejo, Portugal). Five different batches (D382, D383, D396, D495, and D460) of compound A PLGA microspheres were prepared as follows. First, compound A particles were milled down to reduce the particle size of the API. Polymer solution was prepared by dissolving PLGA in methylene chloride. A compound A suspension was prepared by mixing milled compound A particles in the polymer solution. A phase separation agent, dimethicone, was added to induce phase separation under further mixing, forming microspheres. The resulting mixture was then transferred into a container containing a hardening agent, cyclomethicone, to continue hardening the microspheres. The solidified microspheres were collected using a stainless steel screen and rinsed with fresh cyclomethicone. Finally, the collected

microspheres were dried under vacuum to remove residual solvent. They were screened to control size uniformity. All microsphere samples were loaded with approximately 23–24% weight/weight crystalline API.

Laser Diffraction

Particle size distributions of microspheres and API particles were determined with a Sympatec HELOS Laser Particle Size Analyzer. Microspheres were first suspended in the suspension medium that contained squalene and sorbitan monooleate to form a pre-suspension. The pre-suspension was sonicated for about 15 min to break visible aggregation of particles. The pre-suspension was then added dropwise to a test cuvette containing suspension medium, while allowing sufficient mixing time between additions for optical concentration level to stabilize. The addition was continued until an obscuration level between 9% and 12% was reached prior to the performance of the measurement. Samples were prepared in triplicates. Each measurement was repeated three times. Crystalline API particles were determined using the same instrument, except the dry powder sample was sprayed in the air before laser diffraction measurements were taken.

In vitro Dissolution Study

Approximately 4.5 mg of the microspheres were weighed and placed between two 25- μ m screens. The screens were held together by two pieces of donut-shaped Teflon, forming a release cell. Six tubes were prepared for each sample. Each cell was placed into a borosilicate glass tube (25 mm in outer diameter, and 15 cm in length) containing 10 mL of a pH 4.2 phosphate buffer previously equilibrated at 37°C. The tubes were then placed in a tube rotator, which was placed in a convection incubator maintained at 37°C. The tubes were rotated for 4 h, before the solution was removed and analyzed by HPLC. The amount of drug released was measured to derive an initial release rate between 0 and 4 h.

Focused Ion Beam - Scanning Electron Microscope (FIB-SEM)

An Auriga FIB-SEM (Carl Zeiss Microscopy, USA) workstation was used for FIB milling and SEM imaging of individual microsphere cross-sections. The principle of the FIB-SEM technique is illustrated in Fig. 1a, at three stages, before FIB milling, the first FIB-milled cross-section where an SEM image was taken, and the 500th FIB milled cross-section where an SEM image was taken. The intermediate FIB milling and SEM imaging steps are omitted. The sample stage was tilted by 54 degrees, exposing the sample to an ion beam column pointing perpendicularly at the sample. An electron beam concurrently imaged a side view of the sample. For microspheres samples, the microspheres were scattered on a carbon adhesive tape which was fixed on the SEM stub (Fig. 1b). On a selected microsphere (Fig. 1c), cross-sectioning was carried out using 30-keV focused Gallium (Ga) ion beam of various currents. SEM imaging was then conducted at a 54-degree tilt angle, using a 2-keV electron beam. The secondary electron (SE) and energy selective backscattered (EsB) electron detectors were used for SEM imaging. To obtain optimal contrast, each image was collected using a mixture of

40% SE signal and 60% EsB signal. The 2D FIB-SEM scan collected a single image of a cross-section at 20-nm resolution. When a 3D FIB-SEM scan was conducted over an 8–12-h interval, a total of 800–1000 FIB-SEM slices were collected at 20-nm resolution and 20-nm slice thickness. Figure 1d shows the remains of the same microsphere sample as Fig. 1c after FIB-SEM milling and scanning were completed. Due to the non-conductive nature of PLGA, and pharmaceutical materials in general, damage from electron charging and the focused ion beam are common problems requiring careful mitigation. Specially designed sample sputter coatings were used to control charging and maintain sample stability over the hours of automated, continuous FIB milling and SEM imaging. An electron beam with high energy, commonly used in material characterization, was avoided to prevent introducing perturbations that could lead to structural, morphological, or physical form changes on the API, the polymer, or the porosity.

Energy Dispersion X-Ray Spectroscopy (EDS)

An energy dispersive X-ray spectrometer (EDS) (Oxford Instrument, USA) equipped on the Zeiss Auriga FIB-SEM was used to acquire X-ray spectra for elemental identification. To minimize electron–sample interaction volume, hence also improving spatial resolution in elemental analysis, a 5-keV electron beam was used.

Image Analytics

Image analytics were performed using DigiM™ I2S cloud-based image analysis platform (DigiM Solution, USA). The large number of high-resolution 2D images collected from FIB-SEM imaging allowed digitization of the drug sample into a 3D volume. Data from images were expressed in grayscale values. In order to evaluate microstructures of each material phase, image segmentation of material regions was a critical step before these images could be quantified or used for prediction. Drug and porosity phases were segmented using an artificial intelligence (AI)-based image processing algorithm with supervised machine learning (15) in both 2D and 3D. Domain size distributions for API, polymer, and porosity were computed.

FIB-SEM can introduce certain imaging artifacts. Due to the rasterization nature of FIB milling over a plane with materials that were heterogeneous in density, vertical stripes forming a “curtaining” artifact were visible. A Fourier transformation was applied to remove the repetitive stripes after the images were mathematically transformed from the spatial domain to the frequency domain. During FIB milling, 20-nm thickness between slices was specified for each FIB cut. The instrument, however, cannot guarantee that each slice is exactly 20-nm thick. The diameter of the Ga beam itself had some fluctuations, while the sample it milled was composed of inhomogeneous materials. The iterative milling and imaging over a few hours were subjected to small perturbations from either the environment or from the sample itself (*e.g.*, a center of gravity change due to removal of material, de-gassing, and de-hydration in vacuum). These effects caused a fluctuation of thickness ranging from 5 to 20%. The smaller the thickness, the greater the fluctuation percentage. The images from slice to slice were also slightly

misaligned. The thickness fluctuation and slice misalignment are collectively called “drifting artifacts.” As part of the image analytics software workflow, an intensity-match optimization algorithm was applied to correct the drifting artifacts, by iteratively moving two adjacent slices until a maximum intensity overlap was identified. The DigiM™ I2S software was used to accurately correct these imaging artifacts. The result of these corrections is shown in Fig. 6. These corrections were essential to the reliability of image segmentation, and subsequently to the accuracy of any further quantification and modeling. Examples of these artifacts and their corrections on specific samples will be presented in the result section.

Image-Based Pressure-Driven Permeability Simulation

All image-based simulations were conducted using DigiM™ I2S. When 3D FIB-SEM data was collected, pressure-driven permeability along three spatial directions were computed using a voxel-based computational fluid dynamics (CFD) solver. Permeable phases were altered numerically to include porosity only, API phase only, or combined, to study three networks as follows: the network of the API phase, the network of the porosity phase, and the network of a combined phase. These digital experiments allowed the investigation of the degree of connectivity for these three networks, and to understand the impact of porosity.

The permeable phase was reconstructed from the original image resolution, as opposed to being reduced to a pore network model (PNM). Finite volume spatial discretization was directly built on the voxels of the segmented 3D image data. Navier-Stokes equations were then solved with an implicit pressure explicit momentum scheme, using the following government partial differential equations,

$$\begin{aligned} \nabla \cdot \mathbf{u} &= 0 \\ \nabla p &= \mu \nabla^2 \mathbf{u} - (\mathbf{u} \cdot \nabla) \mathbf{u} + \mathbf{f} \end{aligned} \quad (1)$$

where \mathbf{u} is the fluid velocity vector, p is the pressure, μ is the dynamic viscosity, and \mathbf{f} is the body force vector which is set to zero in the simulations reported in this paper. The boundary conditions of the cubic computational domain are specified on the four faces that are perpendicular to the flow direction, and on the interior wall of the pore space, no-flow boundary conditions were used. On the two faces that are parallel to the flow direction, pressure inlet and outlet were specified.

Simulations were conducted on a distributed-memory, parallel cluster with a web browser user interface. After the pressure and velocity fields are solved, Darcy’s law was used to evaluate the absolute permeability for all three directions,

$$k_n = u_n \frac{\mu \Delta x}{\Delta p} \quad (2)$$

where n denotes the direction of flow, and Δx and Δp are the length and pressure drop across the sample, respectively.

Using volume averaging, tensor forms of Equations 4 and 5 can be derived using periodic boundary conditions. The

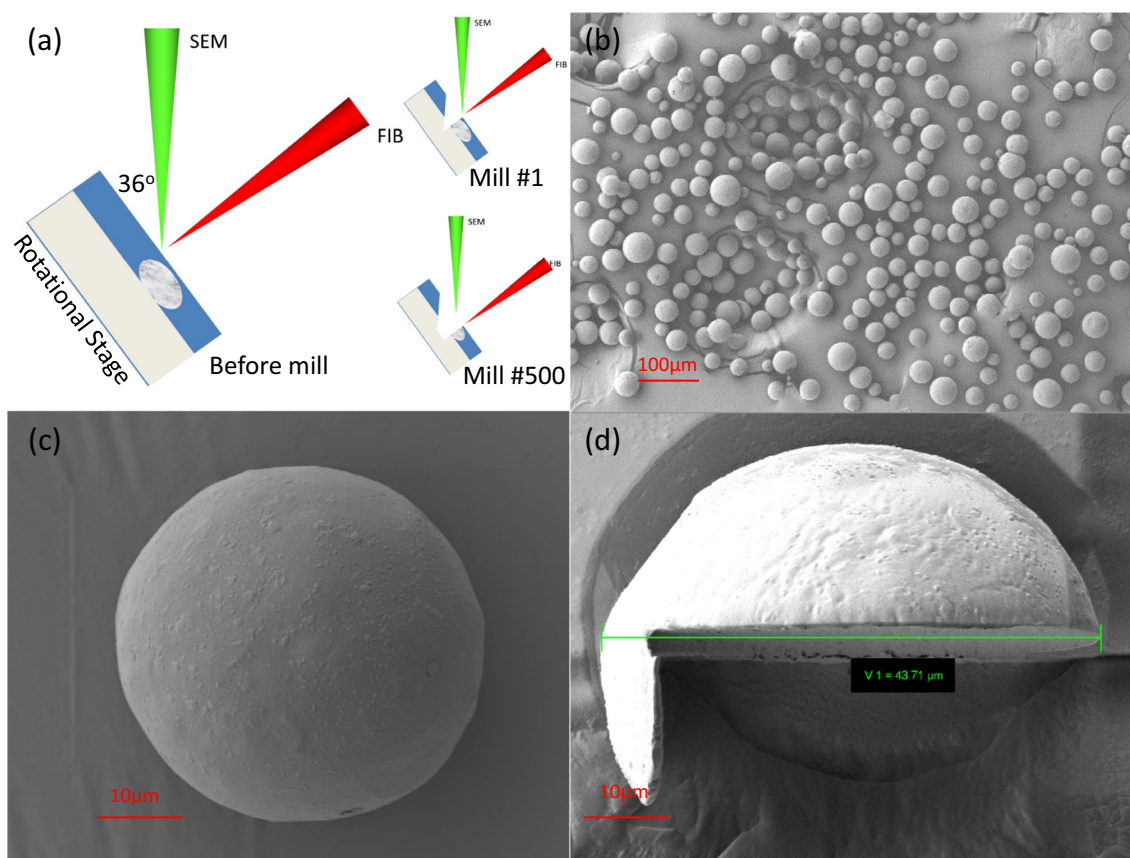


Fig. 1. FIB-SEM overview using sample D396 as an example. **a** FIB-SEM principle diagram. **b** SEM image of microsphere sample on carbon tape. **c** Single microsphere sample. **d** Microsphere sample after FIB-SEM experiment

resulting intrinsic permeability tensor \mathbf{K} does not depend on the flow conditions and describes the anisotropy of the system. Validation results against theoretical models and standard glass bead packaging models are comparable with previous efforts using similar approaches.

When a scalar permeability is needed, the intrinsic permeability tensor collapses into a scalar by taking the three eigen values, k_{e0} , k_{e1} , and k_{e2} , derived from the permeability tensor using

$$k_{mag} = \sqrt{k_{e0}^2 + k_{e1}^2 + k_{e2}^2} \quad (3)$$

The CFD approach to compute permeability is a direct numerical simulation using a finite volume discretization technique (16). In comparison, a PNM approach is a reduced order modeling with simplifications both in pore geometry and consequently in numeric.

Image-Based Release Profile Prediction

With the reconstructed 3D microstructure system in which API particles were dispersed into the polymer matrix, a drug release profile was predicted with a novel numerical method employing percolation theory and Fick's Second Law. The release profile simulation had three components as follows: a percolation simulation, a direct numerical

simulation for the effective diffusivity coefficient, and a release time conversion with a geometry-dependent drug release model.

Percolation Simulation Model

Starting with the 3D reconstruction of the drug API network, the first component of the drug release simulation was a voxel-based percolation simulation using a monolithic release mechanism to simulate the initial release when the PLGA polymer degradation is not significant. Understanding the initial release behavior is an important intermediate step to characterize a complex release system such as a PLGA microsphere. Furthermore, a monolithic model also helps to establish an end member scenario to compare different formulation parameters when PLGA properties are constant.

When a microsphere is in initial contact with the release environment, *e.g.*, body fluids, API molecules in the particles on the surface layer first dissolve into the fluid and diffuse out of the microsphere (17,18). The rate of this initial release is mostly constrained by the solubility limit of the API molecule. In our simulation, interconnected drug particles were released layer by layer from the exterior surface to the interior locations of the drug release system (17,18), following a spherical coordinate system. The discrete increment of drug released from each layer that the model can simulate was dictated by the resolution of the image data. Through this percolation simulation in the spherical coordinate system, the

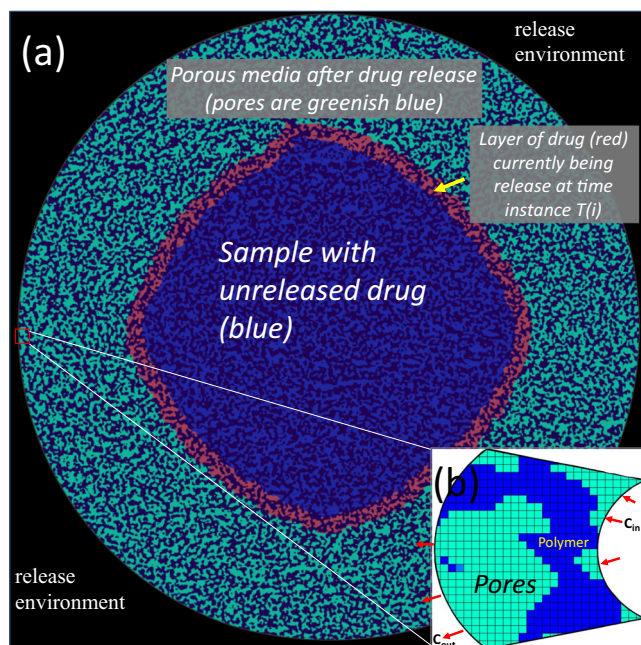


Fig. 2. Monolithic drug release at one time instance; **a** a 2D cross-section of 3D image data of a microsphere sample. **b** Voxel computational cell used for direct numerical simulation of effective diffusivity coefficient. Color legend: black, release environment; dark blue, PLGA polymer; blue, API particles; greenish blue, pores vacated by API release; red, API particles being release at one infinitesimal time instance (exaggerated)

amount of drug released from each outer layer of drug particles that are in contact with dissolution fluid can be evaluated as a fraction of total drug. The microstructures at each intermediate release stage were determined. Figure 2a shows a 2D cross-section of the 3D microsphere sample, at an intermediate release time instance t . To simplify analysis, porosity in the microsphere prior to release was left out intentionally. The space vacated by the API particles became pores filled with dissolution fluid (Fig. 2a), creating a porous polymer media (pores shown in green-blue) between the remaining API (blue) inside the microsphere and the release environment outside the microsphere (black). PLGA polymer domain is displayed in dark blue. The API remaining inside the microsphere was released through the porous polymer media. The thickness of the porous polymer layer thus increased with time, leading to increased tortuosity, decreased effective diffusivity, and a decreased release rate. In Fig. 2a, an infinitesimal drug layer being released at time instance t is displayed in red and exaggerated using several pixels from the actual layer with the thickness of one voxel for better visualization.

This percolation simulation produced a non-dimensional drug release profile, with the voxel distance to microsphere surface as the horizontal axis, and the percentage of the amount of drug released as the vertical axis. During the percolation simulation, each of the intermediate release stage microstructures were generated in 3D. Similar to the depiction of Fig. 2a, these intermediate microstructures included the outer ring of porous media and the inner core with remaining API.

Direction Numerical Simulation Model for Effective Diffusivity Coefficient

In the second step of the release simulation, the porous layer from the intermediate release stage was used as the input of direct numerical simulation for effective diffusivity governed by Fick's Second Law, Equation 4,

$$\frac{\partial C}{\partial t} = D_{\text{bulk}} \nabla^2 C \quad (4)$$

where D_{bulk} is the diffusion coefficient of the API in the solvent, C is the concentration field of the API in the solvent, and t is numerical time in computational integration. Finite volume discretization with Dirichlet boundary conditions was used, where the inlet and outlet concentrations were specified as $C_{\text{in}} = 1.0$ and $C_{\text{out}} = 0.0$. This simulation produced a scalar concentration field throughout the porous layer. Figure 2b illustrates a magnified view of a small region of the simulation domain, where C was solved for all green-blue pixels corresponding to the pore space in a spherical coordinate system of the equivalent effective media. Using the resulting concentration distribution, an effective diffusivity coefficient was derived according to Fick's First Law rearranged in Eq. 5,

$$D_{\text{eff}} = \frac{\vec{j}}{\vec{\nabla} C} \quad (5)$$

where \vec{j} was the mass flux of the API and $\vec{\nabla} C$ was the effective API concentration gradient between inlet and outlet derived using volume integration.

Drug Release Model

In the final step, the numerical, voxel-based release time interval was converted into physical time using modified Higuchi's model (19). The model was expressed in a spherical coordinate system, and rearranged for time conversion in Equation 6:

$$T(i) = \frac{R^2}{2 \left(\frac{C_s}{C_0} \right) D(i)} \left[1 - \left(1 - \frac{M(i)}{M_\infty} \right)^{\frac{2}{3}} - \frac{2}{3} \left(\frac{M(i)}{M_\infty} \right) \right] \quad (6)$$

where T is physical time, i is numerical time in percolation simulation (which determines the porous media domain where Equation 4 was solved, hence is different from t in Equation 4), R is the radius of the microsphere sample, C_s is the total drug amount per unit volume of solution, C_0 is the initial drug amount per unit volume of solution, and $\frac{M(i)}{M_\infty}$ is the fraction of drug released expressed in numerical time i (determined from percolation simulation with the assumption of no change in the solid drug particle density when the particles are still inside the microsphere). $D(i)$ is the effective diffusivity coefficient corresponding to the porous media ring at numerical time i , determined using direct numerical simulation discussed above. Further details of the release simulation method can be found in a published patent application (20).

Degradation of the PLGA material during the release was excluded from this study based on two considerations. First, the initial dissolution rate of the API was assumed to be higher than the polymer degradation rate (21). Furthermore, the formulation under investigation had a fairly high drug loading, providing a percolation network with good interconnectivity. Hence, it was assumed that API diffusion dominated the initial phase of its release. PLGA degradation only became significant at the later phase of the release (22). Second, the inclusion of PLGA degradation complicated the validation of the initial model. The PLGA degradation effect has been studied and will be reported in a separate publication.

RESULTS

Table 1 summarizes the five samples studied in this project, along with the image-based analysis conducted, corresponding drug loading, and other analyzed parameters. The results discussion below uses D396 as the primary example; however, FIB-SEM 2D cross-section, 2D image analysis, and EDS studies were conducted on all five samples.

Due to the small size of the microsphere samples (D_{50} around 50 μm as shown in Table 1), cutting the microspheres mechanically was challenging. The PLGA material matrix was soft and delicate, which further complicated cutting without introducing artifacts or sample damage. Figure 3 demonstrates FIB-SEM as an advantageous cross-section characterization tool. Figure 3a is an SEM image of a cross-section of a microsphere sample prepared by mechanical cutting. Residual surface topology due to mechanical fracturing obscured the details of the microstructure. In comparison, Fig. 3b shows an SEM image of the cross-section prepared by FIB cutting. Different contrasts corresponding to various material phases are clearly and accurately visualized.

The FIB-SEM cross-section image of the microsphere showed characteristic grayscale for each material phase, as indicated in Fig. 3b by areas with different contrast. The grayscale contrasts representing different material phases were further confirmed using EDS. Using D396 as an example, Fig. 4a shows the bottom half of a microsphere cross-section, where spot EDS, area averaged EDS, and elemental map were analyzed. The API molecule contains a hydrochloride counter ion. In Fig. 4b, the abundance of chlorine matching the light gray regions in Fig. 4a confirmed correspondence to the API domain. The dark gray regions absent of chlorine signal corresponded to the PLGA polymer. The API phase also had a higher degree of oxygen than the

PLGA polymer phase, as suggested by the oxygen map (Fig. 4c). Due to the use of an organic solvent containing silicon, it was useful to monitor silicon to determine the existence of any residual silicon solvent and its distribution (Fig. 4d). Both API and polymer phases contained carbon; hence, the porosity space seen in Fig. 4a was confirmed by the carbon map (Fig. 4e). Spot and area EDS on numerous locations were conducted. Four of the spot EDS locations, highlighted as circles in Fig. 1a, are summarized in Fig. 4f. Spots 1 and 3 were on the material phase with bright contrast. Strong Cl signal and the presence of N signal were associated with these unique elements in the API. Spots 2 and 4 did not show N signal, and very weak Cl signal. They were either pure polymer or mostly polymer with a very small amount of API. An area EDS corresponding to the white box in Fig. 4a are also reported in Fig. 4f. The spot and area EDS results were consistent with the EDS map observations. Once phases were confirmed, further imaging on samples did not require EDS analysis, unless a new contrast phase was identified.

EDS in combination with FIB-SEM aided in understanding the distribution of elements, and ultimately various phases, throughout the microsphere sample. Figure 5 shows two EDS measurements, one on the exterior surface of a microsphere, the other on the FIB-SEM cross-section of the same microsphere. The signals of gold and gallium, from the sputter coating and FIB plasma residue respectively, were normalized away. Silicon signal was observed on the exterior surface of the microsphere but not the interior, suggesting remaining residual silicon solvent mostly on the surface. Due to its hydrophobic nature, the presence and distribution of the residual silicon solvent on the exterior could impact the initial water uptake, hence influencing the drug release. On the FIB-SEM cross-section, a slightly stronger chlorine signal was observed than the exterior, suggesting higher density of API per unit area inside the microsphere. The nitrogen signal was also associated with the API.

Through FIB-SEM imaging of sample D396, a 3D volume of the microsphere sample, approximately 20 μm by 20 μm by 12 μm in three dimensions, was digitized with 630 images, which was the basic building unit volume for subsequent analysis and simulation. Figure 6a shows an example of a “curtaining artifact,” which was corrected with the Fourier transformation algorithm (Fig. 6b). Figure 6c shows “drifting artifacts,” which were only obvious on the XZ plane, perpendicular to the imaging plane XY. It was corrected by an intensity-match optimization algorithm (Fig. 6d).

Upon phase confirmation and artifact correction, material phases from FIB-SEM images can be better elucidated and reconstructed. Figure 7a annotates an API particle,

Table 1. Batches of Microspheres Studied

| Column | A | B | C | D |
|-----------|--|--|---------------------|---------------------------------------|
| Sample ID | Microsphere size (μm) D_{10} D_{50} D_{90} | Initial release rate ($\mu\text{g}/\text{mg}/\text{h}$) | Drug loading (w/w%) | Image-based analysis conducted |
| D382 | 34 54 79 | 163 | 23.4 | SEM, FIB, 2D |
| D383 | 36 52 69 | 85 | 23.2 | SEM, FIB, 2D |
| D396 | 32 46 65 | 143 | 23.5 | SEM, FIB, EDS, 3D, release simulation |
| D459 | 31 44 58 | 105 | 23.2 | SEM, FIB, EDS, 2D |
| D460 | 30 41 55 | 172 | 23.6 | SEM, FIB, EDS, 2D |

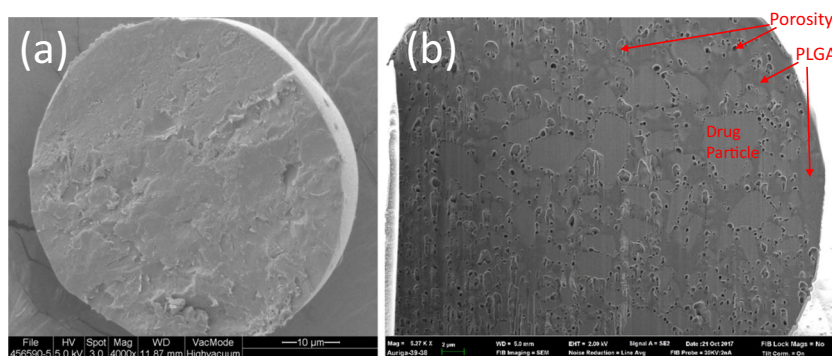


Fig. 3. Comparison of microsphere cross-section technique. **a** Mechanical cut; **b** FIB cut

corresponding to the lightest gray phase, which is distributed in the darker gray polymer matrix. The pores are the darkest in the gray scale. Two types of pores were observed in the microsphere based on their geometry and interaction with the API and polymer. Inter-phase pores were spherical and isotropic, lining the interface between API and polymer domains. These submicron-sized pores were likely associated with the annealing process or drying process. Polymer pores, on the other hand, were observed in the polymer domain. These pores had a high aspect ratio and were anisotropic, likely associated with the pockets of residual solvent and their evaporation. Through a software algorithm using supervised AI learning, API and porosity phases were segmented into red and blue phases respectively as shown in the cross-section image Fig. 7b, corresponding to Fig. 7a. The remaining voxels

corresponding to PLGA polymer were rendered as transparent. Further reconstruction of the API and porosity in 3D, as shown in Fig. 7c and d, found a calculated volume percentage of 41% and 23%, respectively.

Based on the 3D reconstruction of the API phase, API particle size distribution in the microsphere was determined. Table 2 compares the API particle size distributions (PSD) obtained from image analysis with that from laser diffraction measurements. It is important to keep in mind that the PSD measured by laser diffraction was from the sample of raw API material, while the PSD determined by image analysis was based on API particles inside the final microsphere product. Overall, these two particle size measurements are comparable. This confirmed that there was no significant change of original API particle size during the microsphere manufactur-

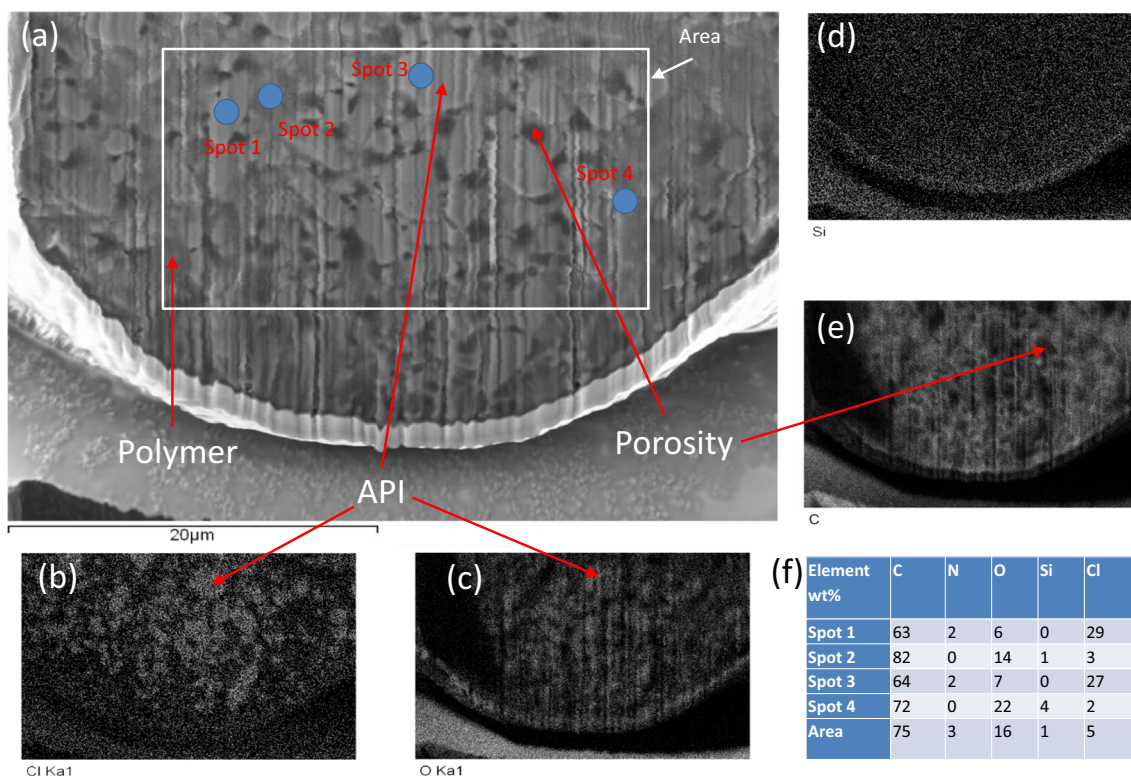


Fig. 4. Confirmation of material phases with EDS map. **a** Cross-section of a bottom half of a microsphere sample. **b** Chlorine distribution map on the same area as **a**. **d** Oxygen map. **c** Silicon map. **e** Carbon map. **f** Spot and area EDS corresponding to the annotations in **(a)**

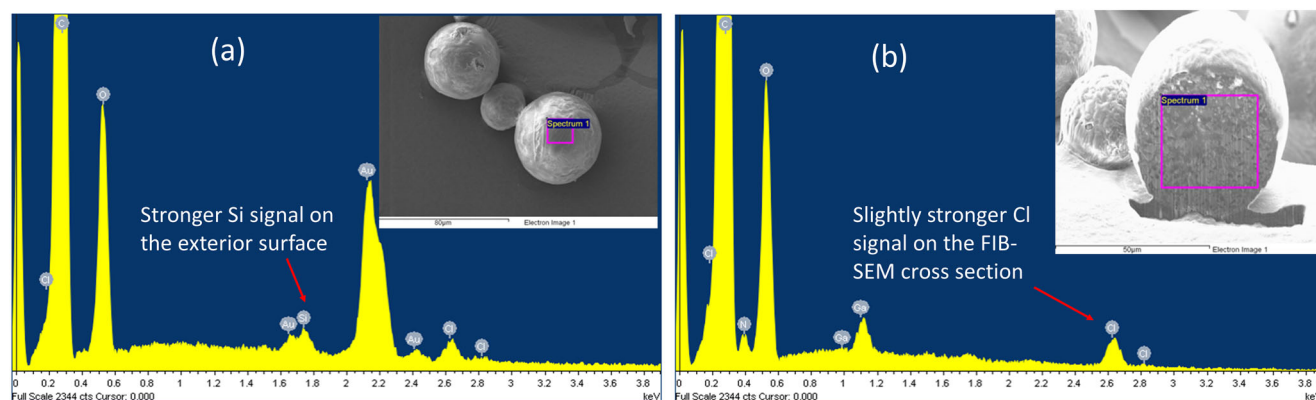


Fig. 5. EDS surface of D396 **a** surface; **b** cross-section

ing process. The results of the D_{90} measurements were particularly interesting. Laser diffraction measurements depended on the dispersion of the sample in the measurement chamber. Aggregation of powder and particle samples likely led to a larger D_{90} measurement with the laser diffraction approach. A more comprehensive comparison of image and laser diffraction PSD results requires additional effort, as making an apple to apple comparison is challenging due to differences in measurement, sample numbers, particle morphology issues, and background calculations and

assumptions. Obtaining a ground truth accuracy can be very challenging in these regards (23).

After image segmentation and phase confirmation, major microstructure properties were calculated. Table 3 compares the microstructure properties computed based on 2D and 3D image data for sample D396. The 2D FIB-SEM analysis provided quick initial characterization of the internal microstructure. Using a relatively large 2D image at one or several cross-sections, the API volume fraction and API particle size distribution were evaluated. These results were comparable

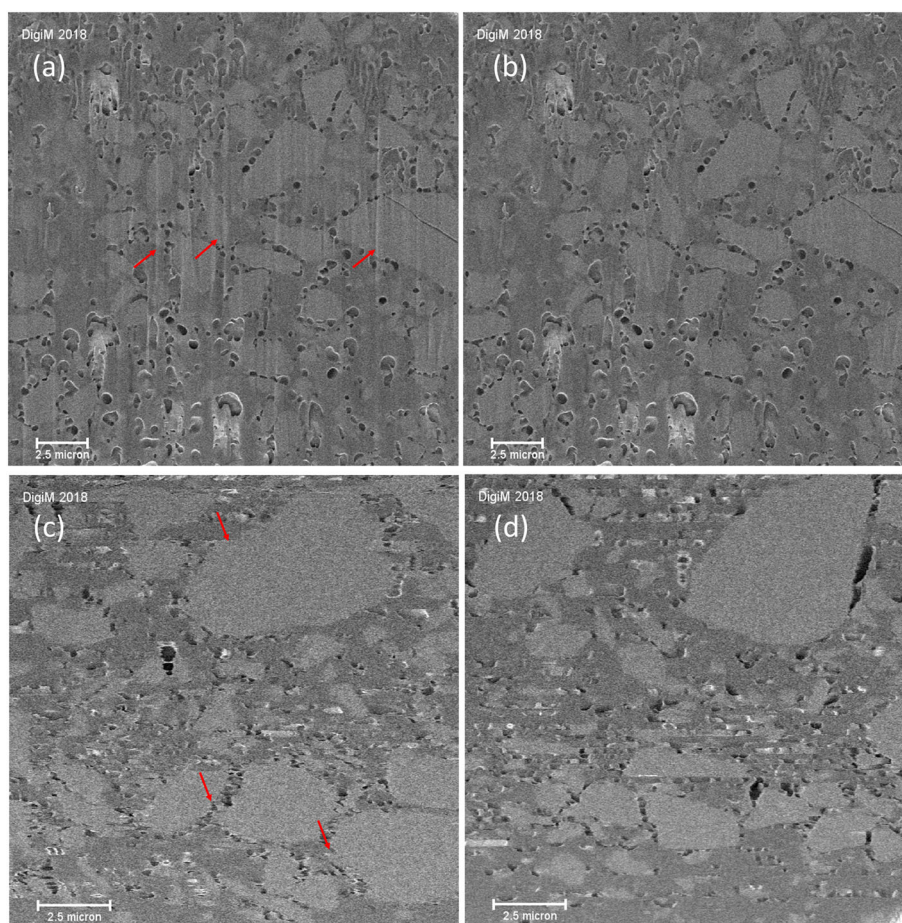


Fig. 6. FIB-SEM imaging artifacts and corrections. **a** XY plane with curtaining artifacts. **b** Same image as **a** with curtaining correction. **c** XZ plane with stage drifting artifacts. **d** Same image as **b** with stage drifting alignment

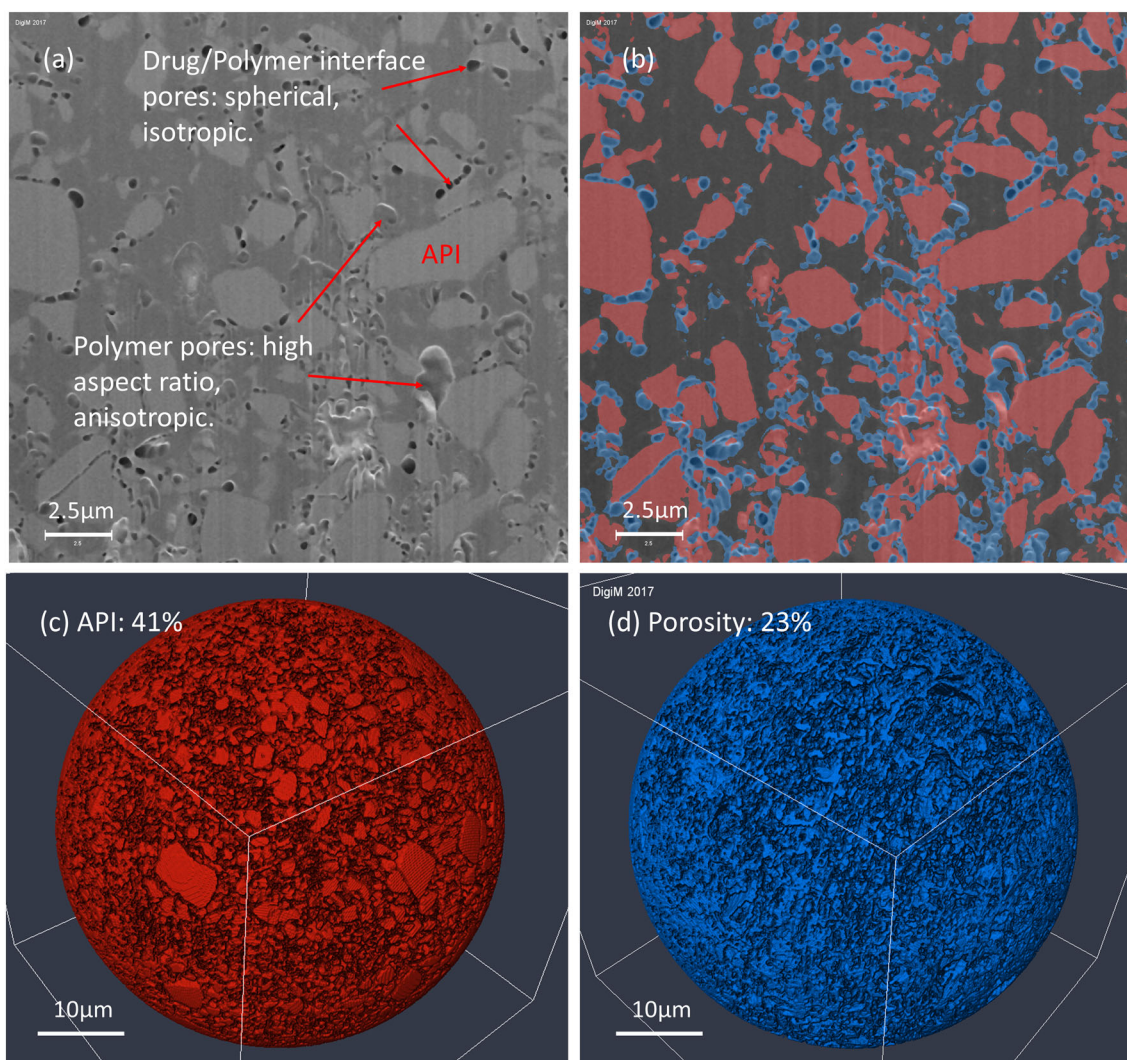


Fig. 7. FIB-SEM image analysis and 3D reconstruction. **a** One example 2D FIB-SEM cross-section image and primary material phase identification; **b** segmentation of API (red) and porosity (blue); **c** 3D reconstruction of API phase; **d** 3D reconstruction of porosity phase

with that from 3D analysis. On the other hand, the 2D study was intrinsically limited in the characterization of transport properties such as diffusivity and permeability. The characterization of microstructure phases with less frequent appearance also required more sampling volume, as available in the 3D FIB-SEM study.

The API phase occupied 41% of the microsphere in volume (Fig. 7b) whereas the porosity was 23% (Fig. 7c). Both phases were found to be distributed homogeneously throughout the microsphere sample. The API volume

fraction reported was converted to a weight percentage of 25.3%, after a density-based volume to weight conversion, and a correction of porosity. Considering uncertainties from microsphere to microsphere variation and lot to lot variation, the drug weight compares reasonably well with the expected 23–24% drug loading.

It is clear in Table 3 that porosity played a significant role in predicted transport properties. The effective diffusivity increased by over a factor of 3 when porosity was considered together with the API domain distribution. Likewise, the permeability increased by a factor of more than one order of magnitude when porosity was considered.

Figure 8 shows several parameters essential to characterize internal microstructures of the microspheres. Figure 8a compares the particle size distributions from three samples. The PSD for these samples, D382, D383, and D396, were very similar. This further confirmed that the API particles in the microsphere product were consistent with the particles from the starting API material. Figure 8a presents the pore size distribution for sample D396. Pore size was a few times smaller than the API particle size. When the API phase and

Table 2. Comparison of API PSD from Image Analysis and Laser Diffraction

| Unit:(μm) | Laser | Image |
|------------------------|-------|-------|
| D ₁₀ | 0.5 | 0.7 |
| D ₅₀ | 1.6 | 1.7 |
| D ₉₀ | 4.3 | 3.3 |

Table 3. AI-Based Image Analysis Summary of Batch D396

| D396 | 2D | 3D |
|---|------------------------|-------------------|
| No. of images | 1 | 630 |
| Image size (number of pixels) | 2048 × 1536 | 1054 × 1045 × 631 |
| API volume fraction (%) | 40 | 41 |
| Porosity (%) | 17 | 23 |
| Number of API particles analyzed | 69 | 342 |
| API D ₁₀ (μm) | 0.85 | 0.65 |
| API D ₅₀ (μm) | 1.85 | 1.70 |
| API D ₉₀ (μm) | 3.85 | 3.25 |
| Pore D ₁₀ (μm) | n/a | 0.42 |
| Pore D ₅₀ (μm) | n/a </td <td>0.64</td> | 0.64 |
| Pore D ₉₀ (μm) | n/a | 0.9 |
| Polymer domain D ₁₀ (μm) | n/a | 0.9 |
| Polymer domain D ₅₀ (μm) | n/a | 1.4 |
| Polymer domain D ₉₀ (μm) | n/a | 2.1 |
| Diffusivity (with API only, fraction of D_{bulk}) | n/a | 0.172 |
| Diffusivity (with Pore only, fraction of D_{bulk}) | n/a | 0.173 |
| Diffusivity (with API and porosity, fraction of D_{bulk}) | n/a | 0.620 |
| Permeability ($\times 10^{-15} \text{ m}^2$) without porosity | n/a | 0.3 |
| Permeability ($\times 10^{-15} \text{ m}^2$) with porosity | n/a | 6.0 |

porosity phase were combined, a virtual phase was generated. Figure 8a suggested that porosity phase did not significantly

alternate the size of this combined phase. Figure 8b shows the distributions of surface area frequency for three scenarios of

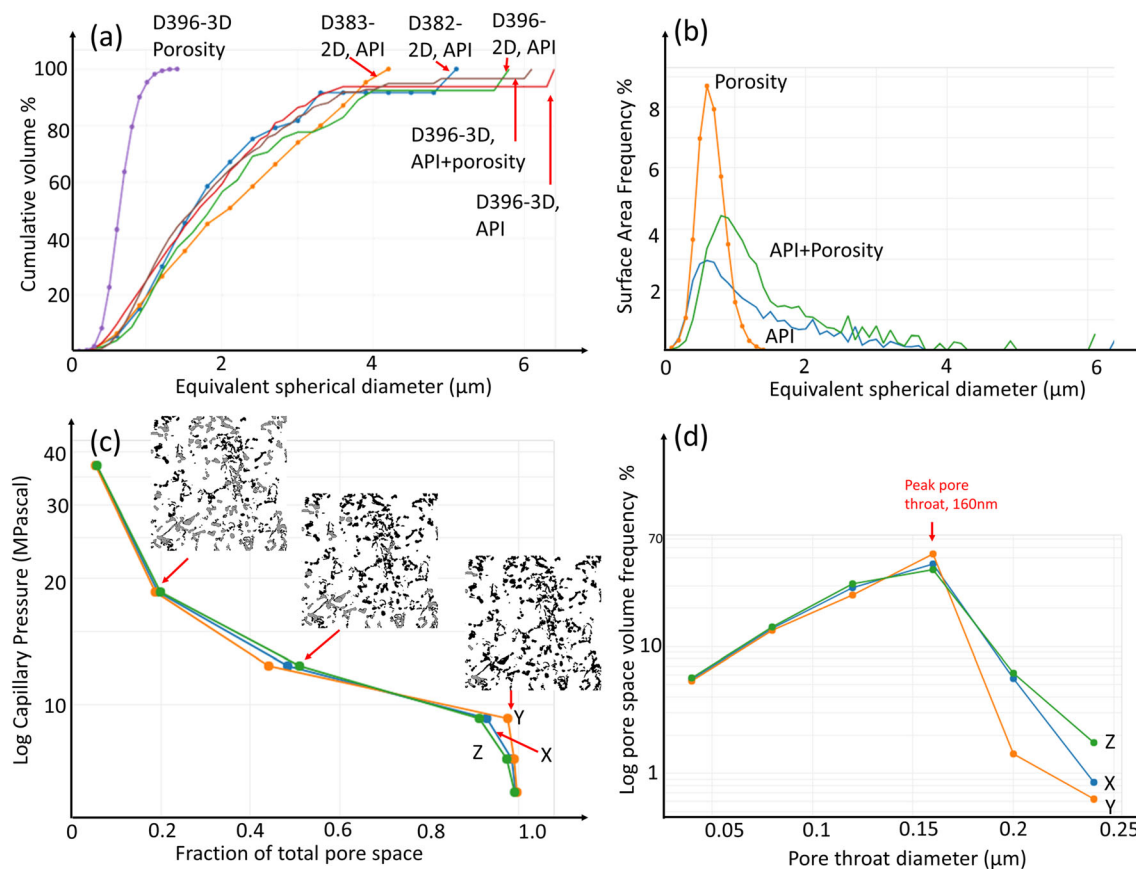


Fig. 8. Summary of quantitative analysis. **a** Domain size distribution comparison among D382, D383, and D396. **b** Surface area distribution of different phases of D396. **c** Capillary pressure distribution from porosimetry simulation on porosity phase of D396 in three Cartesian directions X, Y, and Z. **d** Pore throat distribution corresponding to **c**

sample D396 as follows: porosity phase, API phase, and API combined with porosity phase. It shows that inclusion of porosity notably impacted the distribution of surface area. Peak surface area occurred at 0.9- μm equivalent spherical diameter (ESD) for 4.5% of surface areas, increased from 0.6- μm ESD for less than 3% of surface areas. The surface area is important to consider in evaluating material transport, particularly when surface dynamics such as polymer degradation become significant. Despite having a small effect on the total spherical diameter, inclusion of porosity critically changed the surface area, which explained the significant diffusivity and permeability increases.

Figure 8c and d were computed using a porosimetry module from DigiM I2S™. The module simulated a Mercury Intrusion Capillary Porosimetry (MICP) technique using the Young-Laplace equation (24). Figure 8c shows the pore space being progressively occupied by intruding fluid as capillary pressure increased. The capillary pressure required to penetrate the pore space was dictated by the smallest openings of the pore space, *i.e.*, pore throats. The inserts (black indicates empty pore space; gray indicates pore space occupied by intruding fluid) visualize fluid saturations at three intermediate pressure steps. Figure 8d is the pore throat distribution derived from this porosimetry simulation. Pore throat size peaked at 0.16 μm , four times smaller than the average pore body size of 0.64 μm (Table 3). Pore throat was the limiting factor in mass transfer inside the microsphere, thus having a bigger impact on API release. Porosimetry simulation results in all three directions were comparable, confirming the isotropic character of the pore network of the sample.

Two different batches (D396 and D459) of PLGA microspheres were analyzed by FIB-SEM and compared (Fig. 9). Figure 9a and b show the conventional low-resolution surface SEM for each batch. Similar external

morphology was observed without notable differences. When comparing the corresponding cross-sections prepared by FIB-SEM, Fig. 9c and d, major microstructure differences were apparent, particularly the distribution of API domains. A drug-free zone near the external microsphere surface was observed on sample D459, while more uniform drug distribution was identified throughout the cross-section of sample D396. The existence of the drug-free zone near the external surface requires a longer time for water penetration and offered an explanation to the different release behaviors of formulation D459, which had a retardation in its initial release. The measured initial *in vitro* release rate of D396 (Table 1) was 40% higher than that of D459, as the API particles were closer to the microsphere surface. In addition to the explanation of the release retardation, this comparison confirmed the change in the final drug product which had led to a closer examination on potential changes in the manufacturing process.

Permeability is an important transport parameter, particularly for release systems that are pressure gradient driven. A pressure gradient can be due to osmosis pressure, or from capillary force of dissolution fluid imbibition for strong hydrophilic porous matrix. Table 4 compares the permeability of D396 computed with and without the inclusion of porosity. In both cases, the API phase was assumed to be released, leaving behind a porous network. When porosity was considered, the porosity phase was combined with the API phase, forming a larger porous network. When only the API network was considered, the permeability was fairly small and isotropic in all three directions. When the 23% porosity volume was added to the percolation network, permeability increased by a factor of 20, along with a more anisotropic behavior.

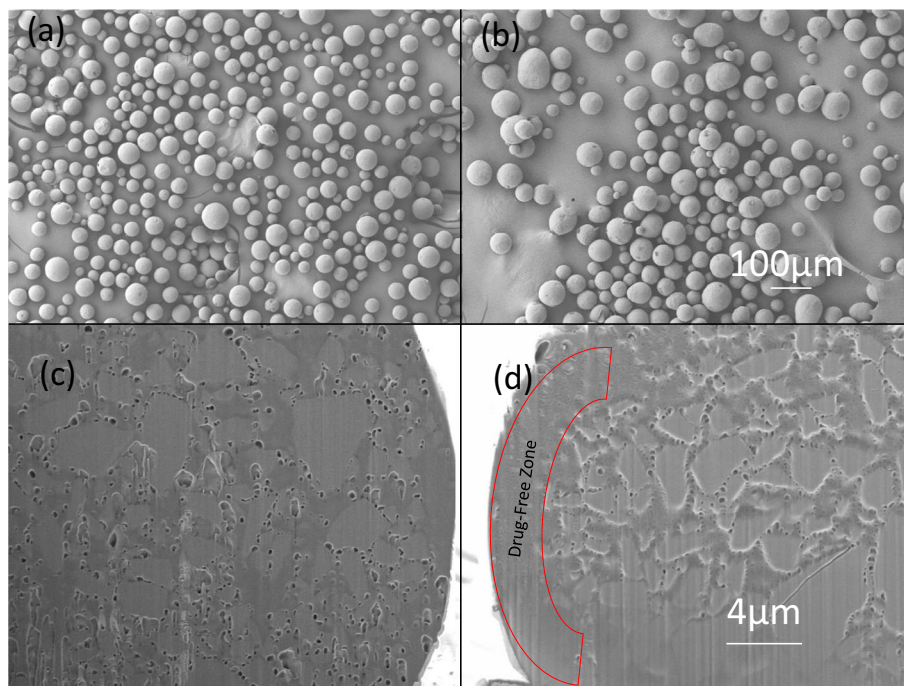


Fig. 9. FIB-SEM cross-section reveals microstructure differences that correlate with different release behaviors. **a** D396 surface SEM. **b** D459 surface SEM. **c** D396 FIB-SEM cross-section. **d** D459 FIB-SEM cross-section

Table 4. Permeability Determination of D396 with 3D FIB-SEM Images

| Permeability ($\times 10^{-15} \text{ m}^2$) | API alone; no porosity considered volume fraction 41% | API and porosity combined, volume fraction 64% |
|---|---|--|
| K_x | 0.2 | 4 |
| K_y | 0.2 | 4 |
| K_z | 0.2 | 2 |
| $K_n = \sqrt{K_x^2 + K_y^2 + K_z^2}$ | 0.3 | 6 |

Release simulations required 3D data and were conducted on sample D396. Figure 10a shows the release profiles predicted. When both the API and porosity were considered, the simulation predicted continuous release up to 3 weeks, consistent with the designed release period of this microsphere drug formulation. The release rate derived from our simulation was 158 $\mu\text{g}/\text{mg}/\text{h}$. It compared reasonably well with the 143 $\mu\text{g}/\text{mg}/\text{h}$ measured experimentally on this particular sample, and with the average release rate of 133.6 $\mu\text{g}/\text{mg}/\text{h}$ of all samples measured experimentally, with a standard deviation of 33.5 $\mu\text{g}/\text{mg}/\text{h}$. For controlled release formulations, it is preferable to reduce porosity to achieve a longer release time. The second release profile in Fig. 10a corresponds to a hypothetical scenario where the porosity of the microsphere sample was numerically eliminated. Instead of reaching 50% drug release in 3 days, it took 16 days to reach the same release amount when porosity was removed from the release percolation network.

Since the release simulation computed effective diffusivity coefficient at each and every time instance, Fig. 10b plots the time varying effective diffusivity coefficient for both release simulation scenarios. The effective diffusivity coefficient decreased sharply during the initial 20% of the release period, due to the rapid increase of the thickness of the porous layer. Once the thickness of the porous layer became large enough, the porous media reached representative length

scale. Further increase of the porous layer thickness did not significantly change the effective diffusivity coefficient.

Figure 11 visualizes an intermediate release time at $T = 5$ days in the monolithic release simulation corresponding to the case where porosity was digitally removed from T0 samples (Fig. 10c). The pores vacated by the released API are shown as blue in 3D and white in 2D cross-sections. Two cross-sections are displayed in Fig. 11. The 3D rendering of the microsphere with pores vacated by the released API were cut open to allow the visualization of the remaining API inside, which is displayed in red on the 2D cross-sections.

DISCUSSIONS AND CONCLUDING REMARKS

Using the PLGA microsphere as an example, this paper has demonstrated an innovative image-based microstructure characterization workflow for controlled release pharmaceutical samples. With careful design of experiments (DoE) factoring in sample representativeness, sample preparation, image resolution, appropriate sample stability control, and artifact mitigation, FIB-SEM is an excellent cross-section tool. FIB-SEM can reveal the internal microstructures of a pharmaceutical sample with unprecedented resolution and accuracy, particularly in comparison to traditional cross-section techniques that involve mechanical methods (*e.g.*, Fig. 3). Information obscured at the micro-scale, which traditional characterization approaches fail to divulge due to a lack of resolution, can be acquired. The EDS detector can collect X-ray signals and identify elemental composition on FIB-SEM cross-section surfaces, providing a correlation between structural contrast and chemical compounds.

While obtaining high-quality images is an important starting point to visualize the internal microstructures of microspheres, vital characterization requires the application of AI image analysis to quantify internal microstructural features. This paper demonstrates, for the first time to the authors' knowledge, that API particles inside the final microsphere product can be verified, quantified, and compared with the starting API material. The analysis can characterize each individual material phase separately or

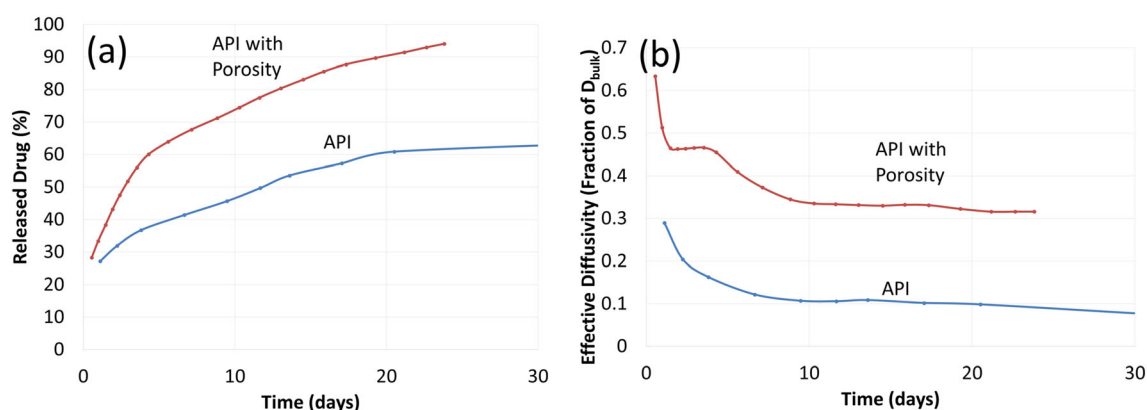


Fig. 10. DigiM I2S predicted monolithic release profile of a microsphere formulation. **a** Simulation of drug release profiles using 3D API percolation network reconstructed from FIB-SEM volume in spherical coordinates, with and without porosity. **b** Predicted effective diffusivity coefficient over a month timeframe

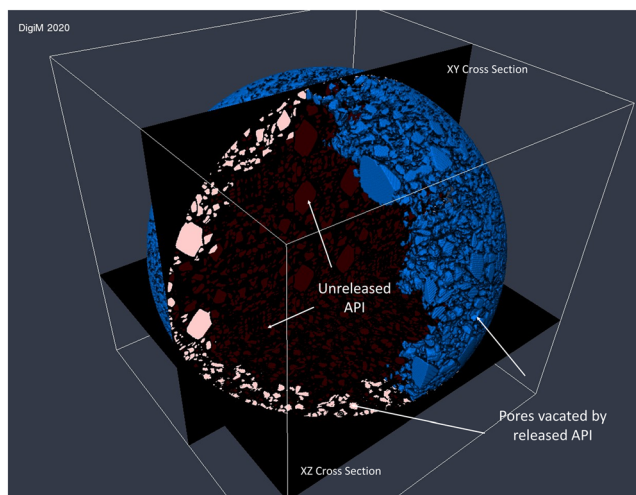


Fig. 11. Visualization of partial API release at $T = 5$ days, where 40% of API was released. The T0 sample of pre-release API phase corresponded to Fig. 7c.

pool them in various combinations in the digital imaging space. Transport properties, such as permeability, effective diffusivity coefficient, and porosimetry, can be computed directly from image data. These properties are difficult, if not impossible, to measure using a physical laboratory approach. All properties have been determined from the same sample, which is not possible in physical laboratory testing. For lab-based tests, specimens of the same batch must be prepared for each and every test. Sample-to-sample measurement uncertainty is thus increased. The accumulated amount of sample required is much higher, which further increases the difficulty and measurement cost.

The microstructures of pharmaceutical samples reconstructed *via* imaging facilitate an unprecedented investigation of release mechanisms and what-if scenarios. Using the image-based characterization framework, the porosity impact on release has been systematically studied. The quantification and classification of porosity provides a direct evaluation of its various impacts on the percolation network, permeability, effective diffusivity, and release profiles. Microporosity in the studied PLGA microspheres samples has been found to have a significant impact on predicted permeability, increasing this parameter by more than an order of magnitude. When the porosity is suppressed, the release of 50% of drug has been extended from 3 days to almost 12 days. In actual formulation and process optimization, this totally pore-free long release would never be achievable. However, the image-based simulation framework predicts what the longest possible release could be. The end-member scenarios provide important guidance to the optimization effort in process engineering. The *in vitro* test in this study is limited to a release interval of only 3 days, restricting evaluation of the controlled release performance and characteristics at late time. In comparison, late stage release profile was obtained with little extra cost using the image-based release modeling approach, reducing cost and time associated with long-lasting *in vitro* tests.

As with any emerging analytical method, challenges and limitations should be noted. Due to the high-resolution FIB-SEM provides, the size of the sample that

can be studied is limited to 50–100 μm in each dimension. As a feasibility study, this project selected several microspheres from each lot of sample, then visually verified consistency in API and porosity microstructures using 2D FIB-SEM cross-sections. 3D FIB-SEM and subsequent analysis were completed on one microsphere sample that was considered to be representative. Due to the limited number of samples studied, the authors caution that any results reported in the paper should be considered suggestive rather than conclusive. For a more comprehensive study, it is important to consider a design of experiment that ensures sample representativeness. Correlative imaging in conjunction with a multi-scale approach is often needed to confirm microsphere to microsphere uniformity. The large data size and intensive nature of computation from both AI image processing and direct numerical simulations increase the demand on computing infrastructure. A cloud framework with flexible and accessible browser user interface and a parallelized backend computing library accelerated by graphics processing unit offers the necessary scalability.

The simulation method based on percolation theory is limited to the release prediction of formulations which have drug loadings high enough to meet or exceed percolation threshold, *i.e.*, the API domain along with the pre-existing porosity forms an interconnected network. When drug loading is low, the API release mechanism changes fundamentally; hence, the polymer excipient matrix behavior has to be considered. For microsphere formulations using biodegradable polymers such as PLGA, the most challenging part in drug release characterization is the dynamic changes of internal structure over the release period. The small domain size and microstructure further complicate the process. A continuous monitoring of the microstructure over the release period will provide additional insight to understand and predict the release, particularly at later stages after the initial release burst dominated by API dissolution. Additional factors impacting drug release, such as the interaction between polymer and API, as well as wettability, require further study.

Due to the unavailability of *in vitro* release profile, it was not possible to validate the full release profile predicted by the model against experimental data at the time of preparing this manuscript. Since only initial release rate was available, the predicted release profile was converted to the corresponding release rate, which matched the experimental release rate within the standard deviation of the experimental data. Although, as discussed previously, the prediction was done on only one microsphere sample, efforts had been made to ensure representativeness to the author's best capacity at the time of study. Some sample to sample variability is expected and to be quantified. Therefore, the preliminary release simulation result reported in this report should be considered as a proof of concept. Continuous effort on validation of the predicted transport parameters and release profile is ongoing with several other long-acting drug development projects including microspheres and implants. This is to further address sample to sample variability the comparison between simulated data and *in vitro* measurements, the impact of polymer degradation through imaging

the microsphere samples before and after the dissolution test (25), and the potential correlation expansion to *in vivo* prediction.

The method reported in this paper can be applied to other controlled release systems including implants, depots, semi-solid formulations, and combination products. Image-based analytics and simulations provide a new set of tools for drug delivery system characterization, design, and manufacturing. The prediction of drug release can provide guidance for formulation design and development very efficiently, which consequently reduces the cost and time for product development and manufacturing.

ACKNOWLEDGMENTS

The authors acknowledge the constructive feedback from the reviewers and editors, and the editorial assistance of Mr. Josh Lomeo from DigiM Solution LLC.

REFERENCES

- Han FY, Thurecht KJ, Whittaker AK, Smith MT. Bioerodable PLGA-based microparticles for producing sustained-release drug formulations and strategies for improving drug loading. *Front Pharmacol.* 2016;7:1–11.
- Phee YS, Park CW, Deluca PP, Mansour HM. Sustained-release injectable drug delivery: a review of current and future systems. *Pharm Technol.* 2010;6:S8–S13.
- Andhariya JV, Choi S, Wang Y, Zou Y, Burgess DJ, Shen J. Accelerated *in vitro* release testing method for naltrexone loaded PLGA microspheres. *Int J Pharm.* 2017;52(1–2):79–85.
- Siepmann J, Siegel RA, Rathbone MJ. *Fundamentals and Applications of Controlled Release Drug Delivery.* Springer; 2012. ISBN 978-1-4614-0881-9
- Poozesh S, Setiawan N, Arce F, Sundararajan P, Rocca JD, Rumondor A, et al. Understanding the process-product-performance interplay of spray dried drug-polymer systems through complete structural and chemical characterization of single spray dried particles. *Powder Technol.* 2017;320:685–95.
- van Apeldoorn AA, van Manen HJ, Bezemer JM, de Bruijn JD, van Blitterswijk CA, Otto C. Raman imaging of PLGA microsphere degradation inside macrophages. *J Am Chem Soc.* 2004;126(41):13226–7.
- Gamble JF, Terada M, Holzner C, Lavery L, Nicholson SJ, Timmins P, et al. Application of X-ray microtomography for the characterization of hollow polymer-stabilised spray dried amorphous dispersion particles. *Int J Pharm.* 2016;510(1):1–8.
- Yost E, Chalus P, Zhang S, Peter S, Narang AS. Quantitative X-ray micro-computed tomography assessment of internal tablet defects. *J Pharm Sci.* 2019;108(5):1818–30.
- Wang Y, Wertheim DF, Jones AS, Coombes AG. Micro-CT in drug delivery. *Eu J Pharm Biopharm.* 2010;74(1):41–9.
- Zhao A, Rodgers VG. Using TEM to couple transient protein distribution and release for PLGA microparticles for potential use as vaccine delivery vehicles. *J Control Release.* 2006;113(1):15–22.
- McCarthy D. A closer look at PLGA microspheres. *In Focus.* 2010;17:18–24.
- Gu B, Sun X, Papadimitrakopoulos F, Burgess DJ. Seeing is believing, PLGA microsphere degradation revealed in PLGA microsphere/PVA hydrogel composites. *J Control Release.* 2016;228:170–8.
- Orloff J, Swanson L, Utlaut M. *High resolution focused ion beams: FIB and its applications.* Springer; 2002. ISBN 978-0-306-47350-0
- Goldstein J, Newbury DE, Joy DC, Lyman CE, Echlin P, Lifshin E, et al. *Scanning electron microscopy and X-ray microanalysis.* Springer; 2003. ISBN 978-0-306-47292-3
- Zhang S, Byrnes AP, Jankovic J, Neilly J. Management, analysis, and simulation of micrographs with cloud computing. *Microsc Today.* 2019;27(2):26–33.
- Byrnes AP, Zhang S, Canter L, Sonnenfeld MD. Application of integrated core and 3D image rock physics to characterize Niobrara chalk properties including relative permeability with boundwater effect. *Proceedings of Unconventional Resources Technology Conference, 2017; URTeC Manuscript 2670963.*
- Kamaly N, Yameen B, Wu J, Farokhzad OC. Degradable controlled-release polymers and polymeric nanoparticles: mechanisms of controlling drug release. *Chem Rev.* 2016;116:2602–63.
- Ford Versypt AN, Pack DW, Braatz RD. Mathematical modeling of drug delivery from autocatalytically degradable PLGA microspheres – a review. *J Control Release.* 2013;165(1):29–37.
- Siepmann J, Siepmann F. Modeling of diffusion controlled drug delivery. *J Control Release.* 2012;161(2):351–62.
- Zhang S. System and method for computing drug controlled release performance using images. U.S. Patent App., Pub. No. 2019/0108322 A1, published Apr. 11, 2019.
- Makadia HK, Siegel SJ. Poly lactic-co-glycolic acid (PLGA) as biodegradable controlled drug delivery carrier. *Polymers (Basel).* 2011;3(3):1377–97.
- Engineer C, Parikh J, Raval A. Hydrolytic degradation behavior of 50/50 poly lactide-co-glycolide from drug eluting stents. *Trends Biomater Artif Organs.* 2010;24(3):131–8.
- Gamble JF, Dawson N, Murphy D, Theophilus A, Kippax P. A proposal for an alternative approach to particle size method development during early-stage Small molecule pharmaceutical development. *J Pharm Sci.* 2019;108:3515–20.
- Hilpert M, Miller CT. Pore-morphology-based simulation of drainage in totally wetting porous media. *Adv Water Resour.* 2001;24(3–4):243–55.
- Timmins P, Desai D, Chen W, Wray P, Brown J, Hanley S. Advances in mechanistic understanding of release rate control mechanisms of extended-release hydrophilic matrix tablets. *Ther Deliv.* 2016;7(8):553–572.

Publisher's Note Springer Nature remains neutral with regard to jurisdictional claims in published maps and institutional affiliations.